Annals of Nuclear Energy 157 (2021) 108224

Contents lists available at ScienceDirect

Annals of Nuclear Energy

journal homepage: www.elsevier.com/locate/anucene

Thermal neutron scattering measurements and modeling of yttrium-hydrides for high temperature moderator applications ☆

Chris W. Chapman [a,*], Kemal Ramić [b], Xunxiang Hu [c], Jesse M. Brown [a], Goran Arbanas [a], Alexander I. Kolesnikov [d], Douglas L. Abernathy [d], Luke Daemen [d], Anibal (Timmy) J. Ramirez-Cuesta [d], Yongqiang Cheng [d], Matthew B. Stone [d], Li (Emily) Liu [b], Yaron Danon [b]

[a] Reactor & Nuclear Systems Division, Oak Ridge National Laboratory, Oak Ridge, TN, 37831, United States
[b] Rensselaer Polytechnic Institute, Gaerttner LINAC Center, 3021 Tibbits Ave., Troy, NY 12180, United States
[c] Material Science & Technology Division, Oak Ridge National Laboratory, Oak Ridge, TN, 37831, United States
[d] Neutron Scattering Division, Oak Ridge National Laboratory, Oak Ridge, TN, 37831, United States

ARTICLE INFO

Article history:
Received 6 October 2020
Received in revised form 20 January 2021
Accepted 26 February 2021

Keyword:
Thermal neutron scattering
Yttrium hydride
Temperature dependent effective potential

ABSTRACT

Thermal neutron scattering measurements of yttrium hydride from 5 to 1,200 K were conducted to determine the change in inelastic scattering as a function of temperature and to probe for anharmonic effects. Additionally, measurements on samples of YH_x from x = 1.62 to 1.90 were done to determine the effects of varying hydrogen concentration on the inelastic spectra. Changes in temperature affected the inelastic spectra in unanticipated ways, indicating that there are anharmonic effects, whereas hydrogen concentration did not significantly affect the inelastic spectra. These measurements were compared against the ENDF/B-VIII.0 thermal scattering files of YH_2, as well as new thermal scattering files created by using the stochastic temperature-dependent effective potential (s-TDEP). Both libraries were found to be in good agreement with the experimental data at lower temperatures. At higher temperatures, the s-TDEP method is better at predicting the experimentally observed softening of phonon modes in acoustic and optical regions.

1. Introduction

Hydrogen is an ideal moderator material for use in nuclear reactor applications, and water is the most commonly used moderator. However, its application for high-temperature reactor systems above 400 °C is limited to extremely high-pressure systems. In contrast, metal hydrides are uniquely suited for high-temperature reactor systems. Historically, ZrH was the preferred metal hydride for nuclear reactor applications due to its low absorption cross section, negative prompt temperature reactivity coefficient, and general availability. Yttrium hydride was not widely used due to the unavailability of high-purity yttrium and its much higher cost. Today, high-purity yttrium metal is available as an industrial metal, making it attainable. As a result, yttrium hydride has become the moderator of choice for high-temperature reactors due to its superior thermal stability indicated by its lower equilibrium hydrogen partial pressure and the higher attainable hydrogen concentration at high temperature (>1,100 K) (Wang and Olander, 1995; Begun et al., 1980). This is why yttrium hydride is being developed under various US Department of Energy (DOE) programs to serve as the moderator for microreactors and small modular reactors (DOE, 2017). One of these programs—the Transformational Challenge Reactor (TCR) program, which launched in 2019 at Oak Ridge National Laboratory (ORNL)—was created to leverage advances in novel materials, processing, and modeling to significantly reduce the time needed to iterate from conceptual design to nuclear regulatory qualification. Yttrium hydride was selected as the moderator material for the TCR program (Betzler et al., 2020).

Moderating materials require special care when simulating thermal neutron scattering in neutron transport codes because, unlike traditional nuclear data that treat the nucleus as an isolated

* Corresponding author.
E-mail address: chapmancw@ornl.gov (C.W. Chapman).

https://doi.org/10.1016/j.anucene.2021.108224
0306-4549/

free gas atom, the de Broglie wavelength of the neutron becomes comparable with the interatomic distances of the materials, and crystal structure effects must be considered. Specific files (i.e., thermal scattering libraries) are required to describe these interactions. The ENDF/B-VIII.0 (Brown et al., 2018) library for yttrium hydride was developed with the implicit assumption that the phonon density of states (DOS) does not significantly change as a function of temperature (Zerkle and Holmes, 2017). This library was found to be in good agreement with room temperature total cross section measurements, but no comparison with differential scattering measurements was made nor were temperatures other than room temperature considered. Additionally, no effort was made to quantify the anharmonic effect known to exist in metallic hydrides (Elsässer et al., 1996) or to determine whether this effect would impact differential scattering measurements or the total cross section. Additionally, the hydrogen concentration dependence of the neutron scattering properties of YH_x are unknown, although it is critically important for the optimized design of reactors that use YH_x moderators with various hydrogen concentration.

The purpose of this work is twofold. The first purpose is to provide differential scattering cross section measurements that can be used to compare against the existing ENDF/B-VIII.0 yttrium hydride library. These measurements were obtained at the ORNL Spallation Neutron Source (SNS) at various temperatures by using YH_x with various hydrogen concentrations. The second is to explore new methods for generating a thermal neutron scattering library to account for these anharmonic effects on double differential neutron scattering cross sections. To accomplish this, the stochastic temperature-dependent effective potential (s-TDEP) method (Hellman et al., 2011; Hellman and Abrikosov, 2013; Hellman et al., 2013; Shulumba et al., 2017) was used to calculate these features. A robust thermal neutron scattering library verified by critical experiments will facilitate more accurate neutron transport calculations for optimal reactor core designs.

Section 2 describes the yttrium hydride fabrication process, and Section 3 provides a brief overview of thermal neutron scattering theory, simulation, and experimental techniques. Section 4 discusses the experimental results and their comparison against the available ENDF/B-VIII.0 and s-TDEP simulations. Section 5 presents concluding thoughts and comments about future work.

2. Yttrium hydride fabrication

Yttrium hydride samples with various H/Y atomic ratios were fabricated through the direct interaction of ultrahigh purity metallic yttrium (nominal 99.99%, purchased from American Elements) and hydrogen at elevated temperature. Carefully matching the processing temperature and hydrogen partial pressure in the retort gives rise to the desired hydrogen concentration informed by the well-established thermodynamics of the Y-H binary system. Final hydrogen gas pressure was determined based on the desired H/Y atomic ratios of the hydrides. More details regarding the fabrication of the yttrium hydride are available in Hu et al. (2020). Each synthesised yttrium hydride sample, YH_x, is labeled by the number of hydrogen atoms *per* yttrium atom of the sample, *i.e.*, x = H/Y, as determined by using the weight change method[1]. X-ray diffractometry (XRD) was also performed to identify the phases presented within each sample. A representative XRD pattern (i.e., $YH_{1.62}$) is shown in Fig. 1. The alpha phase yttrium (hexagonal close-packed crystal structure) containing hydrogen solid solution, and delta

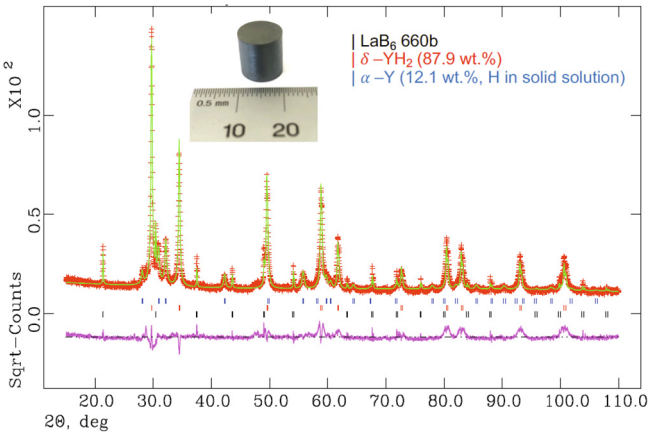

Fig. 1. XRD pattern of $YH_{1.62}$ and Rietveld refinement fit. The picture of a $YH_{1.62}$ rod (10 mm in diameter, 15 mm tall) is also shown. LaB6 is the standard material mixed with hydride powder in XRD and is not included in the yttrium hydride.

phase yttrium dihydride ($YH_{\sim 2}$ face-centered cubic structure) (Khatamian et al., 1980) are both found in the fabricated hydride samples. The hydride samples with higher H/Y atomic ratios have a larger weight fraction of delta-phase yttrium hydride. The weight fractions of α-Y containing H solid solution and δ-$YH_{\sim 2}$ determined from XRD measurement are shown in Table 1 for the studied samples. Here samples YH_x are listed as a function of the atomic ratio (number of hydrogen atoms per yttrium atoms) as opposed to concentration (number of hydrogen atoms per total atoms).

The inelastic neutron scattering (INS) experiments were performed on three instruments at SNS—the Wide Angular-Range Chopper Spectrometer (ARCS) (Abernathy, 2008), the Fine-Resolution Fermi Chopper Spectrometer (SEQUOIA) (Granroth et al., 2010), and the Vibrational Spectrometer (VISION) (Seeger et al., 2009)—and their descriptions are given in Section 3.2. For SEQUOIA experiments, two bulk yttrium hydride rods that were 10 mm in diameter and 15 mm tall—$YH_{1.62}$ and $YH_{1.86}$—were fabricated first and then crushed into fine powder. To mitigate the hydrogen release at elevated temperature, an Al sample holder was used to contain the powder sample. The Al sample holder consists of an Al plate and cover (Al-6063). A specially designed Al gasket was used to enable the gas-tight sealing of the final assembly. The yttrium hydride powder was loaded in the area of 30 × 40 × 0.5 mm. An opening was available at the bottom of the Al plate for inserting a heating rod to enable the uniform temperature distribution across the sample holder, which was attached to the hot stage adapter at the bottom-loading close-cycle refrigerator (CCR) at SEQUOIA. During neutron scattering experiments, the sample in the sealed holder and Al heat shield were in a vacuum. This setup provides low neutron scattering background and allowed the sample temperature to be controlled from T = 5 to 800 K. Fig. 2 shows pictures of the sample holder assembly before the holder was sealed. Similar Al sample holders were used for VISION measurements. Unlike the SEQUOIA measurements, the bottom heating element attachments were not needed due to the He exchange gas in the top-loading CCR of VISION in which measurements were done at T = 5 and 293 K. These sample holders could be directly mounted to the CCR of the SEQUOIA and VISION instruments.

For the high-temperature ARCS measurement (up to 1,200 K), a thin-wall low B quartz tube (0.46 mm wall thickness and 9.07 mm inside diameter) was used to contain the 0.11 mm yttrium hydride foil. The 0.1 mm metallic yttrium foil was first loaded in the quartz tube, and then the assembly was placed in the retort of the TCR bulk metal hydriding system for hydrogen loading (Hu et al., 2020). The quartz tubes were sealed after the successful fabrication

[1] Note that Y-H binary phase diagrams in literature are plotted as a function of hydrogen concentration, that is, $x/(1+x)$. To illustrate, a maximum hydrogen concentration of yttrium hydride in its alpha phase at room temperature is approximately 0.19 (Fu et al., 2018; Khatamian and Manchester, 1988), corresponding to $YH_{0.235}$ in stoichiometric notation.

Table 1
XRD analysis of yttrium hydride samples for the thermal neutron scattering measurements at room temperature. Hydrogen ratio in the first column was determined from the weight change during the hydriding process.

Samples	Weight fraction of α-yttrium containing hydrogen solid solution (%)	Weight fraction of δ-$YH_{\sim 2}$ weight pct (%)
$YH_{1.62}$	12.1	87.9
$YH_{1.68}$	11.6	88.4
$YH_{1.74}$	9.0	91.0
$YH_{1.86}$	4.2	95.8
$YH_{1.87}$	2.7	97.3
$YH_{1.90}$	2.1	97.9

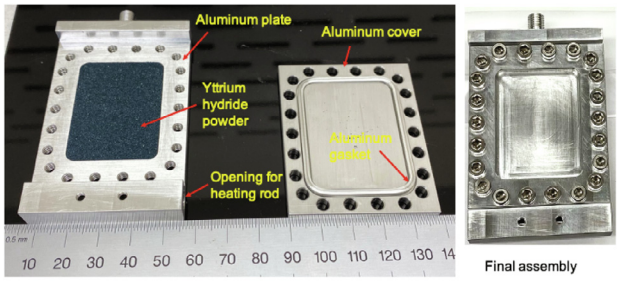

Fig. 2. The Al sample holder parts and the final assembly.

of yttrium hydride. During the measurement, the quartz tube containing yttrium hydride foil was placed in a V sample holder and mounted in the MICAS furnace installed at ARCS (Niedziela et al., 2017). Fig. 3 shows the thin-wall quartz tubes that contain yttrium hydride foils.

3. Thermal neutron scattering

3.1. Theory

The theory of thermal neutron scattering experiments is extensively described in MacFarlane and Kahler (2010) and in the authors' previous work (Chapman et al., 2021; Ramic et al., 2018, 2019). Here, the authors focus on the most important parts of these studies. In the typical neutron scattering experiment, time-of-flight data are transformed to *S(Q,E)*, which is the dynamic structure factor, and $\hbar Q$ and E are the neutron momentum and energy transfer. The double differential scattering cross section (DDXS) can be represented as:

$$\frac{d^2\sigma}{d\Omega dE} = \frac{\sigma_b}{4\pi}\frac{\mathbf{k}\prime}{\mathbf{k}}S(Q,E), \tag{1}$$

where $\mathbf{k}\prime$ and $\mathbf{k}$ are wavevectors of final and initial neutron states, respectively; Ω is the solid angle; and σ_b is the bound scattering cross section. In the ENDF/B-VIII.0 format, DDXS is represented as:

$$\frac{d^2\sigma}{d\mu dE} = \frac{\sigma_b}{4\pi k_B T}\sqrt{\frac{E_f}{E_i}}e^{-\beta/2}S(\alpha,\beta), \tag{2}$$

where E_i and E_f are the incident and scattered neutron energies, respectively; μ is the cosine of the scattering angle; k_BT is the equilibrium temperature in eV; α and β are unitless momentum and energy transfer, respectively; and $S(\alpha,\beta)$ is the scattering law. The transformation between $S(Q,E)$ and $S(\alpha,\beta)$ is as follows:

$$S(Q,E) = \frac{S(\alpha,\beta)}{k_B T e^{-E/(2k_BT)}}, \quad \alpha = \frac{\hbar^2 Q^2}{2Am_n k_B T}, \quad \beta = \frac{-E}{k_B T}, \tag{3}$$

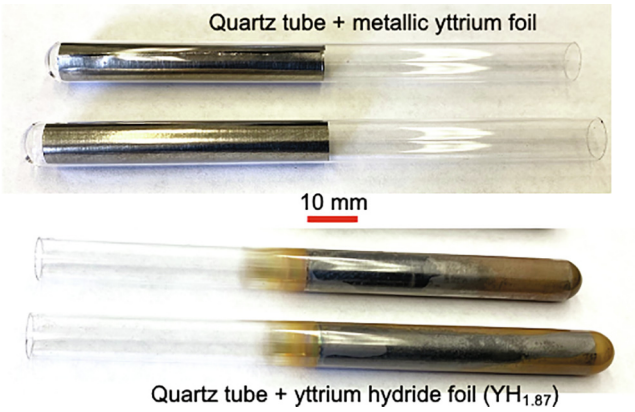

Fig. 3. Quartz tubes containing yttrium foils and yttrium hydride foils.

where m_n is the neutron mass, and A is the ratio of the scattering atom mass to the neutron mass. By using the LEAPR module of NJOY2016 (MacFarlane and Kahler, 2010), the $S(\alpha,\beta)$ can be calculated from the phonon spectrum, or *DOS*, by using:

$$S(\alpha,\beta) = \frac{1}{2\pi}\int_{-\infty}^{\infty} e^{i\beta\hat{t}}e^{-\gamma(\hat{t})}d\hat{t}, \tag{4}$$

with:

$$\gamma(\hat{t}) = \alpha\int_{-\infty}^{\infty} P(\beta)\left[1 - e^{-i\beta\hat{t}}\right]e^{-\beta/2}d\beta, \tag{5}$$

where $\hat{t}$ is the time measured in units of $\hbar/k_BT$ seconds, and $P(\beta)$ is dependent on the phonon spectrum, $\rho(\beta)$, as follows:

$$P(\beta) = \frac{\rho(\beta)}{2\beta\sinh(\beta/2)}. \tag{6}$$

3.2. Experimental techniques

Three instruments—ARCS, SEQUOIA, and VISION—were used to measure the INS of the yttrium hydride samples at SNS. ARCS and SEQUOIA are direct geometry time-of-flight spectrometers in which an incident neutron energy is specified and a spectra of final energies and scattering angles is measured. Both instruments use a Fermi chopper to define the energy of the incident neutrons. This is done by rotating the chopper at a specific frequency and phase relative to the timing of the pulsed source to allow through only the desired neutron energy. The neutrons then interact with the sample material, and the scattered neutrons are measured downstream at the detector bank.

For both instruments, incident energies of 45, 180, and 600 meV were selected for measurement. The incident energies of 45 and 180 meV were chosen based on previous calculations and measurements of the phonon DOS (Udovic et al., 1994), which show significant contributions below 30 meV and between 100 to 150 meV. The 600 meV incident energy was chosen to measure multiple phonon scattering. For the purposes of these experiments, there are three primary differences between ARCS and SEQUOIA. The detector bank at SEQUOIA covers scattering angles from −30 to 60° in the horizontal plane and ±18° in the vertical plane. By comparison, ARCS covers angles from −28 to 135° in the horizontal plane and −27 to 26° in the vertical plane. Another difference is in the energy range and energy resolution available with these instruments. ARCS allows for incident neutron energies between 20 to 1,500 meV with a resolution at the elastic peak between 3–5%, whereas SEQUOIA can measure incident energies between 4 to 6,000 meV with an energy resolution between 1 to 5%. Finally,

Table 2
Sample information for thermal neutron scattering measurements.

SNS instrument	Samples	Sample form	Sample fixture	Mass [g]	Temperature [K]
SEQUOIA	$YH_{1.62}$	Powder	Al plate and cover	0.6966	5
	$YH_{1.86}$			0.7020	5, 295, 550, 800
VISION	$YH_{1.62}$			0.6966	5, 293
	$YH_{1.74}$			0.6684	
	$YH_{1.86}$			0.7020	
	$YH_{1.90}$			0.7696	
ARCS	$YH_{1.68}$	0.1 mm hydride foil	Thin-wall quartz tube	1.6681	295, 550, 800, 900, 1,000, 1,100, 1,200
	$YH_{1.87}$			1.8937	

ARCS allows the high-temperature MICAS furnace to be used for measurements up to 1,600 °C.

VISION is an indirect geometry vibrational spectrometer. Unlike a direct geometry spectrometer, VISION shines a white beam of neutrons on the sample, and the final energy is selected by setting analyzer pyrolytic graphite crystals at specific angles that correspond to scattered energies of 4 meV. This results in a constant relative energy resolution of $\Delta E/E$ = 1.5%. There are two detector banks at VISION: a forward scattering bank at 45° (low Q), and a back scattering bank at 135° (high Q).

At SEQUOIA, $YH_{1.86}$ was measured at 5, 295, 550, and 800 K. Additionally, $YH_{1.62}$ was also measured at 5 K. This additional measurement was done to investigate the differences in hydrogen concentration on the DDXS. $YH_{1.87}$ was measured at ARCS at temperatures of 295, 550, 800, 900, 1,000, 1,100, and 1,200 K. The higher temperatures represent the range of temperatures expected for normal TCR operations, and a description of any changes as a function of temperature is needed to accurately model the reactor. VISION was used to further analyze the differences in hydrogen concentration by measuring $YH_{1.62}$, $YH_{1.74}$, $YH_{1.86}$, and $YH_{1.90}$ at 5 and 293 K. A table summarizing the sample characteristics for each experiment is shown in Table 2.

3.3. Simulation techniques

The calculation of the phonon spectrum is not a straightforward task, and over time, different methodologies that use first principles or molecular dynamics (MD) have been presented. Codes such as PHONON (Parlinski, 2007) and Phonopy (Togo and Tanaka, 2015) use density functional theory (DFT) to perform lattice dynamics calculations in harmonic and quasi-harmonic approximation. More recently, codes such as MDANSE (Goret et al., 2017), Alamode (Tadano et al., 2014), and PhononA (Parlinski, 2018) were developed to address anharmonicity in lattice dynamics calculations. In this work, anharmonicity and the temperature dependence of the phonon spectrum were addressed via the TDEP method (Hellman et al., 2011; Hellman and Abrikosov, 2013; Hellman et al., 2013), which is a collection of tools for finite temperature lattice dynamics. The main algorithm of the code extracts interatomic force constants (IFCs) from sets of displacements and forces them by fitting them to coefficients in an effective lattice dynamical Hamiltonian. Lattice dynamics theory shows that the displacement of the atom from its equilibrium position in the lattice changes the potential energy of the lattice. As the temperature changes, it disorders the lattice, changing the atomic positions of all atoms in the lattice. The total potential energy of the lattice can be modeled as a Taylor expansion of potential energy contributions at each atom's position in the lattice. For an atom i whose position is defined as displacement u_i from a equilibrium position $R_i + \tau_i$, in which R_i is the lattice vector and τ_i is the position in lattice:

$$\mathbf{r}_i = \mathbf{R}_i + \boldsymbol{\tau}_i + \mathbf{u}_i, \tag{7}$$

and the potential energy can be expended in terms of displacements as:

Table 3
Calculated densities of YH_2 at 295 K using different exchange–correlation functionals.

Functional	Density (g/cm^3)	Standard deviation (g/cm^3)
LDA	4.42	2.71E-02
GGA-PBE	4.19	3.21E-02
GGA-PBE DFT-D2	4.38	2.81E-02
GGA-PBE DFT-D3-BJ	4.33	3.19E-02
GGA-rPBE	4.10	2.92E-02
GGA-rPBE DFT-D3-BJ	4.35	2.98E-02
GGA-BLYP	4.06	2.82E-02
GGA-BLYP DFT-D2	4.36	3.15E-02
GGA-PBEsol	4.32	2.73E-02
GGA-AM05	4.31	2.87E-02

Table 4
The summary of lattice constants for YH_2 obtained from AIMD and QHA. The units are in Å.

Method	5 K	295 K	550 K	800 K
AIMD	5.1641	5.1886	5.2091	5.2339
QHA	5.2038	5.2100	5.2241	5.2441

$$U(\{\mathbf{u}\}) = U_0 + \sum_i \sum_\alpha \Phi_i^\alpha u_i^\alpha + \frac{1}{2!}\sum_{ij}\sum_{\alpha\beta}\Phi_{ij}^{\alpha\beta}u_i^\alpha u_j^\beta + \frac{1}{3!}\sum_{ijk}\sum_{\alpha\beta\gamma}\Phi_{ijk}^{\alpha\beta\gamma}u_i^\alpha u_j^\beta u_k^\gamma + \frac{1}{4!}\sum_{ijkl}\sum_{\alpha\beta\gamma\delta}\Phi_{ijkl}^{\alpha\beta\gamma\delta}u_i^\alpha u_j^\beta u_k^\gamma u_l^\delta + \ldots, \tag{8}$$

where U_0 is the potential energy of the static lattice, and $\alpha\beta\gamma\delta$ are Cartesian indices. The coefficients of a Taylor series expansion, denoted by Φ, that are derivatives of potential energy with respect to the displacements of atoms are called *IFCs* or *Born-von Kármán force constants*. The basic idea of effective phonon theories is to sample a potential energy surface and produce an effective Hamiltonian. The crystal Hamiltonian is equal to:

$$\widehat{H} = U_0 + \sum_i \frac{\mathbf{p}_i^2}{2m_i} + \frac{1}{2!}\sum_{ij}\sum_{\alpha\beta}\Phi_{ij}^{\alpha\beta}u_i^\alpha u_j^\beta + \frac{1}{3!}\sum_{ijk} \times \sum_{\alpha\beta\gamma}\Phi_{ijk}^{\alpha\beta\gamma}u_i^\alpha u_j^\beta u_k^\gamma + \ldots, \tag{9}$$

where p_i is the momentum, Φ_{ij} are the second-order IFCs, and Φ_{ijk} are third-order IFCs. The potential energy surface can be sampled by Born–Oppenheimer MD (i.e., ab initio MD [AIMD]) or by stochastic sampling (Shulumba et al., 2017). Both methods produce displacements and forces that can be fitted to the effective Hamiltonian. For this work, stochastic sampling was used, as introduced in Shulumba et al. (2017) and described in more detail in Kim et al. (2018) in which nuclear quantum effects were also studied. In this work, only phonon spectra from second-order IFCs were studied, but the follow-up paper that is in preparation will study the effects of including third- and fourth-order IFCs while also including

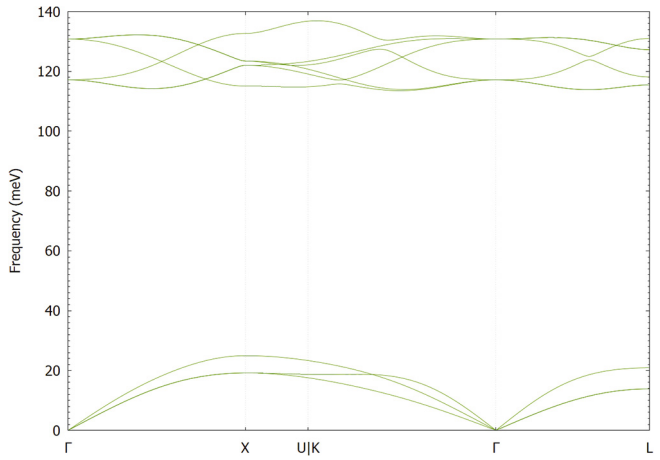

Fig. 4. The calculated phonon dispersion lines at 5 K for YH_2 from the "phonon_dispersion_relations" module of TDEP. The symbols on the *x*-axis represent the high symmetry points in the first Brillouin zone.

nuclear quantum effects, which are highly prelevant for materials that include hydrogen.

The approach to sampling the potential energy surface had two parts. The first part was calculating temperature-dependent lattice constants, and the second part was calculating forces generated from temperature-dependent stochastic samples. In both cases, VASP was used, which is a package for performing ab initio quantum–mechanical MD simulations with pseudopotentials or the projector-augmented wave method and a plane wave basis set (Kresse and Hafner, 1993; Kresse and Furthmüller, 1996; Kresse and Furthmüller, 1996). For the force calculations, the GPU port of VASP (Hacene et al., 2012; Hutchinson and Widom, 2012) was used.

A supercell of 96 atoms was used to calculate temperature-dependent lattice constants. Two methods were used; one calculated lattice constants from AIMD, and the second used the quasi-harmonic approximation (QHA), as implemented in Phonopy. Although the obtained values for lattice constants from AIMD were slightly undercalculated, the method served as a check for which the exchange–correlation function should be used for

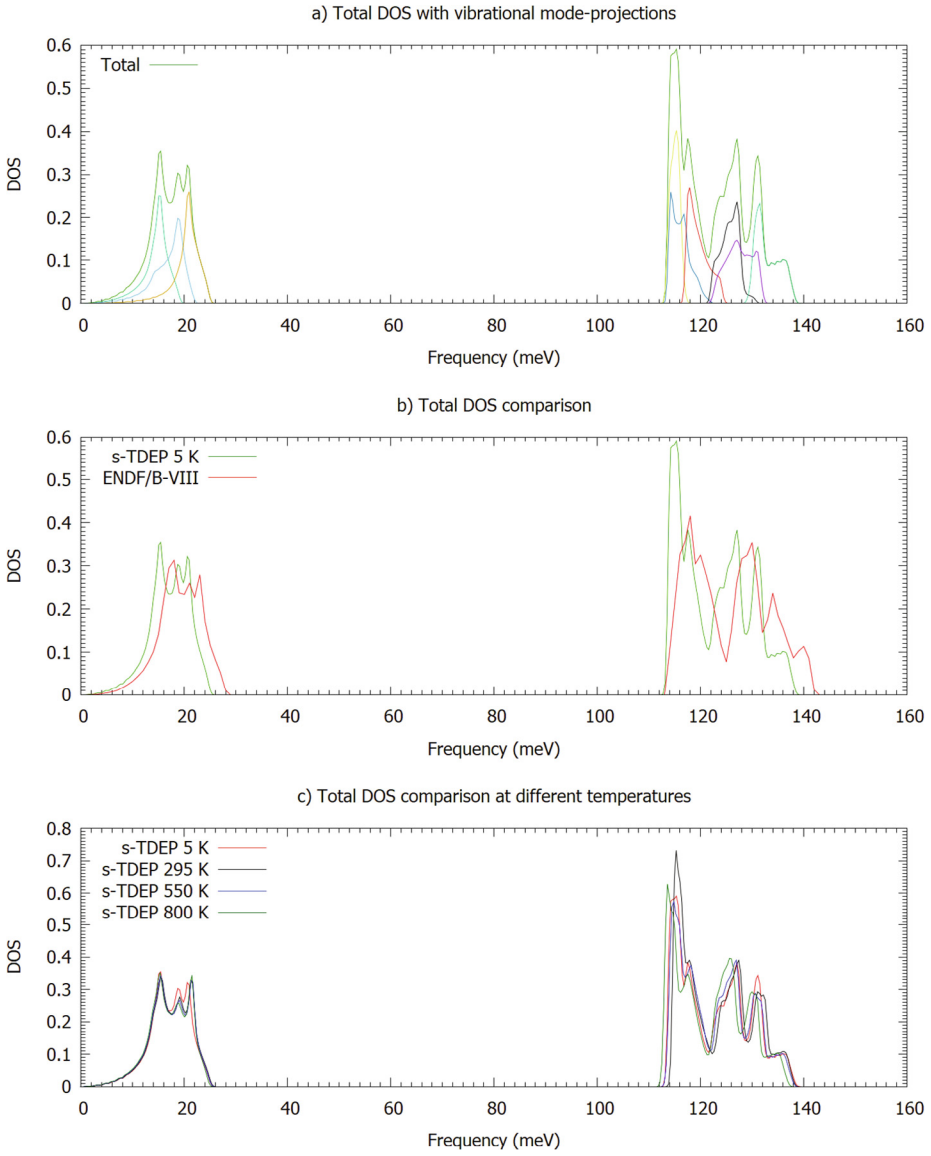

Fig. 5. (a) The calculated phonon spectrum at 5 K. The green line corresponds to the total phonon DOS, and the other lines correspond to each vibrational mode. (b) The comparison between ENDF/B-VIII.0 phonon spectrum and s-TDEP phonon spectrum at 5 K. (c) The temperature dependence of s-TDEP-calculated phonon spectra.

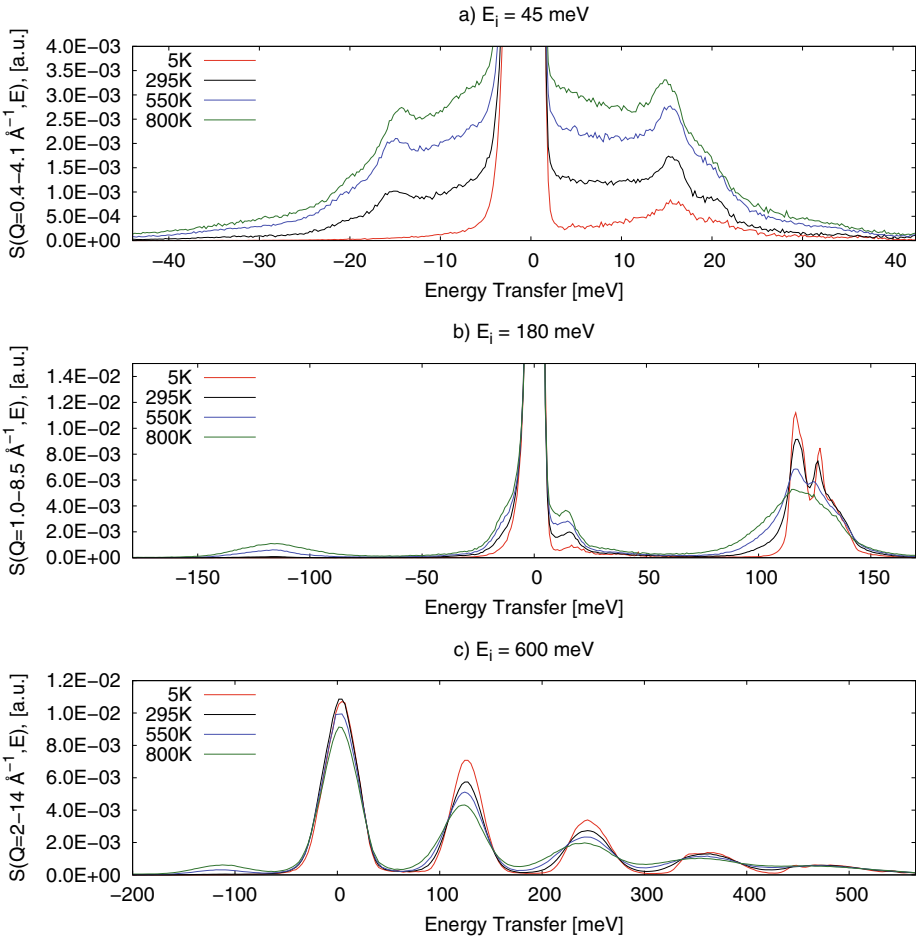

Fig. 6. Temperature comparison of the Q-integrated dynamic structure factor of $YH_{1.86}$ measured at SEQUOIA: (a) E_i = 45 meV, (b) E_i = 180 meV, and (c) E_i = 600 meV.

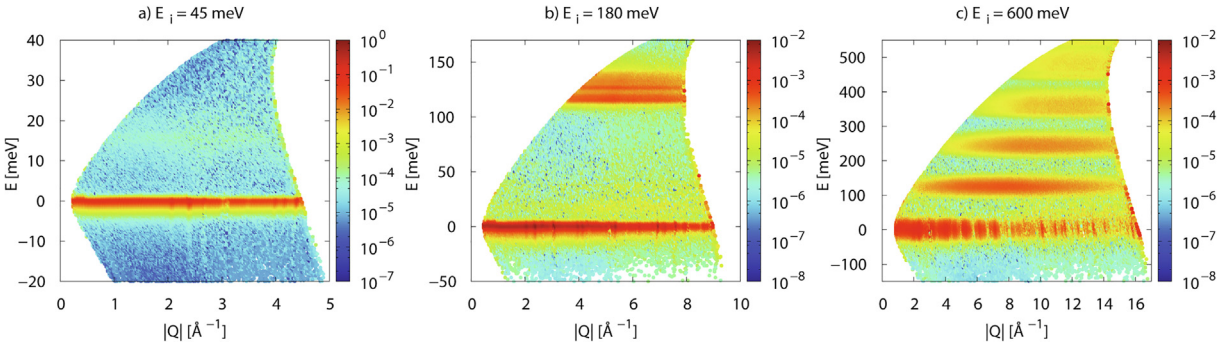

Fig. 7. 2D mesh of the dynamic structure factors of $YH_{1.86}$ measured at SEQUOIA at 5 K for three incident energy measurements.

calculating forces. According to the "YH_2 Crystal Structure" data sheet (Villars, 2016), the density of YH_2 at 295 K is 4.27 g/cm^3. A set of 20 picoseconds simulations were performed with a time step of 1 femtosecond and NPT calculations with different exchange–correlation functionals at 295 K where the density was calculated at each time step. The summary of calculated densities is shown in Table 3, where the standard deviation for calculated density is determined over the 20 picoseconds NPT calculations for each functional.

The GGA-AM05 functional was chosen for subsequent calculations. To calculate the lattice constant at 5 K, the system was cooled over a period of 10 picoseconds, equilibriated for an initial 2 picoseconds, and then further equilibriated for 20 picoseconds to calculate the lattice constant. The lattice constant at 550 K was calculated by heating the 295 K structure over 10 picoseconds, with an initial equailibriation over 2 picoseconds followed by 20 picoseconds to calculate the lattice constant. Then, by using the same procedure, the lattice constant at 800 K was determined by heating from 550 to 800 K. The summary of lattice constants obtained from AIMD and QHA is shown in Table 4.

Lattice constants calculated via the QHA method—for which the value at 5 K was in line with the experimentally obtained value of 5.2032 Å at 90 K in Daou and Vajda (Daou and Vajda, 1992)—were used to generate stochastic samples by the "canonical_configuration" module of TDEP at temperatures that correspond to the measurements. For force calculations, a 4 × 4

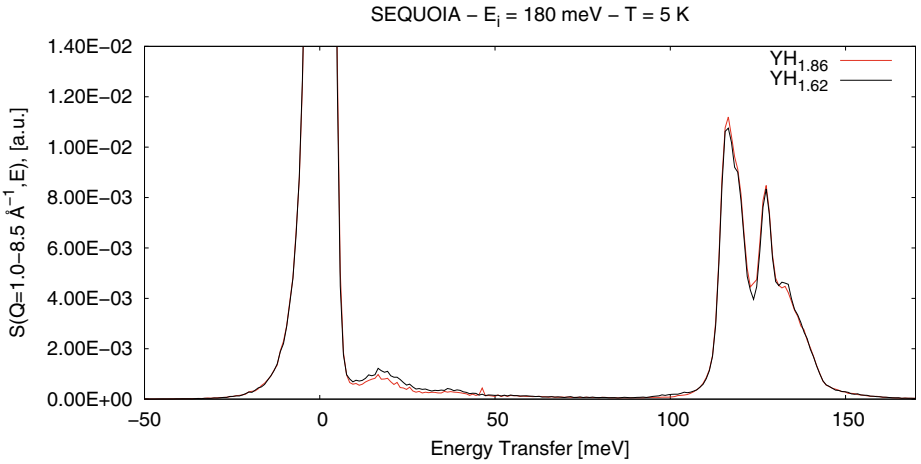

Fig. 8. Hydrogen concentration comparison of the *Q*-integrated dynamic structure factor of $YH_{1.62}$ and $YH_{1.86}$ for E_i = 180 meV at 5 K measured at SEQUOIA.

× 4 supercell was used with a primitive unit cell that had three atoms—one yttrium and two hydrogen atoms—for a total of 192 atoms. Force calculations were performed using a 5 × 5 × 5 k-points grid in VASP with the following parameters: IBRION = −1, ISIF = 2, Prec = Accurate, ENCUT = 500, EDIFF = 1.0E-9, ISMEAR = 2 with SIGMA = 0.01, IALGO = 38, ADDGRID = .TRUE., and LREAL = Auto flags. For the most accurate force calculation, it is desirable to use the LREAL = .FALSE. flag, but due to the use of a GPU VASP port, which only accepts LREAL = Auto or .TRUE., the authors had to settle with slightly less precise force calculations. They tried to compensate for this by performing an extra iteration of s-TDEP force calculations. *s-TDEP* is an iterative procedure that continues until the IFCs are converged. The authors started with two samples generated by the "canonical_configuration" module of TDEP, performed VASP forces calculations, and extracted IFCs by using TDEP. This was followed by generating four new stochastic samples by "canonical_configuration" with the IFCs from the two samples in a previous iteration. After VASP force calculations, 4 + 2 IFCs were extracted, eight new stochastic samples were generated, and this procedure

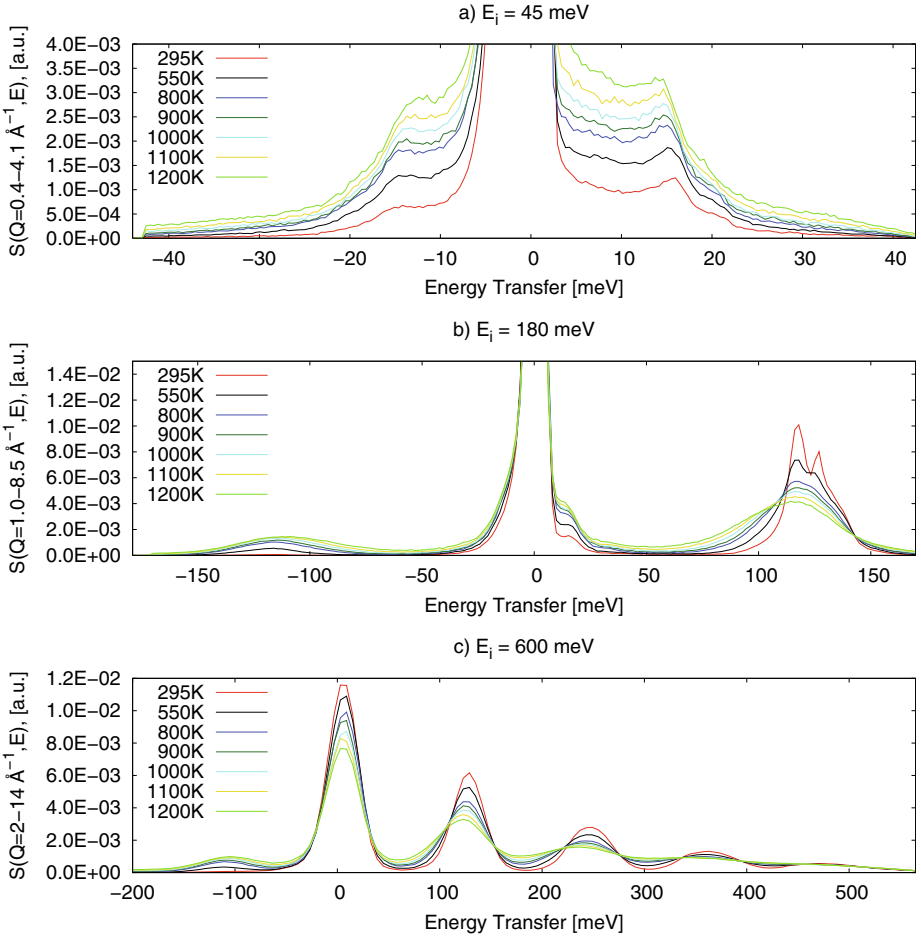

Fig. 9. Temperature comparison of the *Q*-integrated dynamic structure factor of $YH_{1.87}$ measured at ARCS.

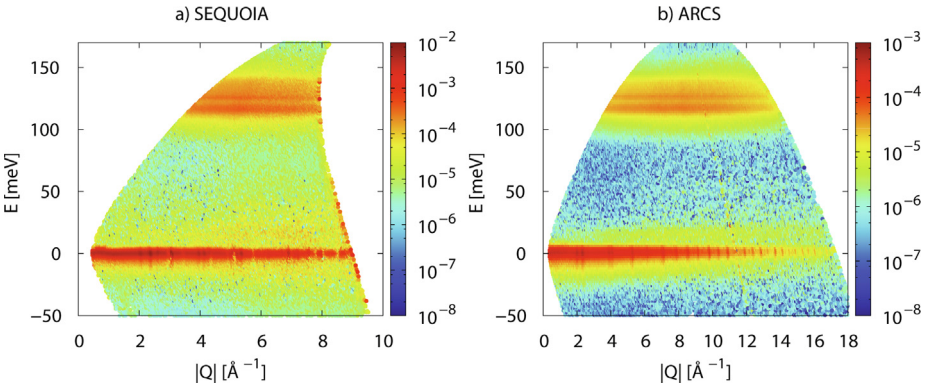

Fig. 10. Instrument comparison of the 2D mesh of the dynamic structure factors at 295 K measured for E_i = 180 meV neutrons of (a) $YH_{1.86}$ at SEQUOIA and (b) $YH_{1.87}$ at ARCS.

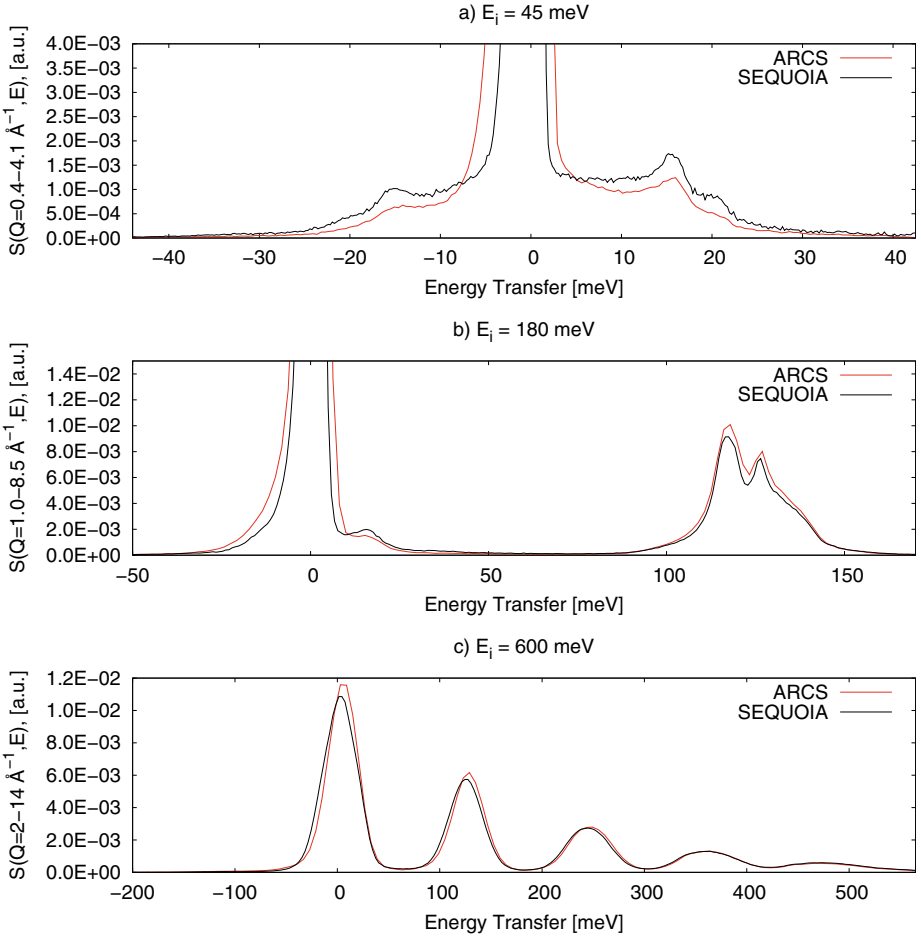

Fig. 11. Instrument comparison of the *Q*-integrated dynamic structure factors at 295 K for $YH_{1.86}$ at SEQUOIA and $YH_{1.87}$ at ARCS.

was repeated until the IFCs converged. Complete IFC convergence was observed on the seventh iteration (i.e., 254 VASP force calculations).

Phonon dispersion relations can be calculated by using the "phonon_dispersion_relations" module of TDEP from second-order IFCs by calculating the eigenvalues and eigenvectors of the dynamical matrix over the Brillouin zone:

$$\omega_{\mathbf{q}}^2 \boldsymbol{\epsilon}_{\mathbf{q}} = \Phi(\mathbf{q}) \boldsymbol{\epsilon}_{\mathbf{q}}, \tag{10}$$

where $\omega_{\mathbf{q}s}^2$ are the eigenvalues, $\boldsymbol{\epsilon}_{\mathbf{q}s}$ are eigenvectors, and the partial derivatives of the dynamical matrix are equal to:

$$\frac{\partial \Phi_{ij}(\mathbf{q})}{\partial q_\alpha} = \sum_{\mathbf{R}} i R_\alpha \frac{\Phi_{ij}(\mathbf{R})}{\sqrt{m_i m_j}} e^{i\mathbf{q}\cdot\mathbf{R}}. \tag{11}$$

The calculated phonon dispersion lines along the high symmetry points in the first Brillouin zone are shown in Fig. 4. There are three lower energy acoustic modes and six higher energy optical modes. Vibrations of yttrium atoms are mostly responsible for acoustic modes, and vibrations of hydrogen atoms are dominant for optical modes.

The phonon DOS can also be calculated with the "phonon_dispersion_relations" module of TDEP by using:

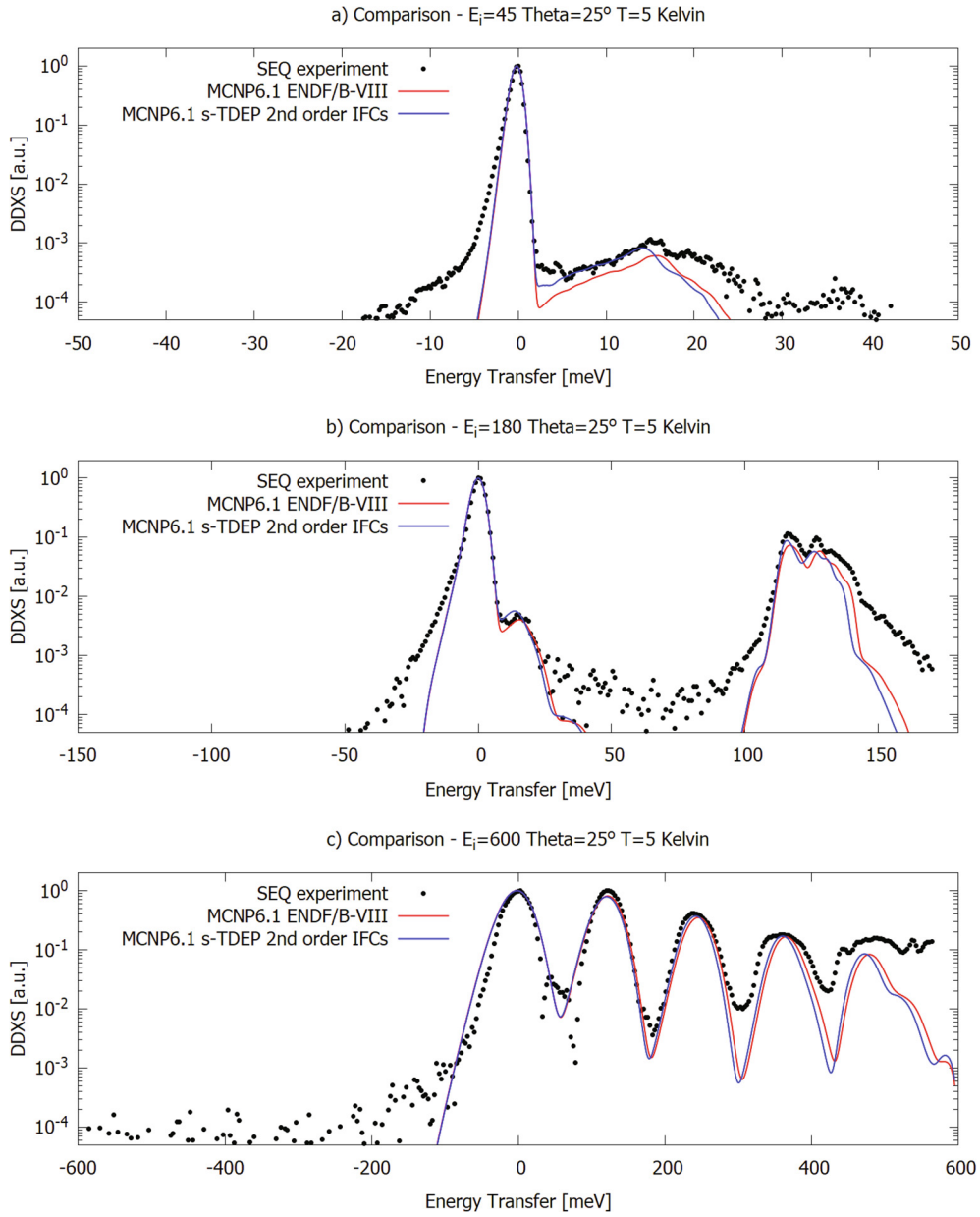

Fig. 12. DDXS comparison between ENDF/B-VIII.0 and s-TDEP against SEQUOIA measured data at 5 K, 25° scattering angle, and 45, 180, and 600 meV incident energies.

$$g_s(\omega) = \frac{(2\pi)^3}{V} \int_{BZ} \delta(\omega - \omega_{\mathbf{q}s}) d\mathbf{q}, \tag{12}$$

for each vibrational mode *s*. The atomic contribution for each atom *i* is:

$$g_i(\omega) = \frac{(2\pi)^3}{V} \sum_s \int_{BZ} \left| \epsilon^i_{\mathbf{q}s} \right|^2 \delta(\omega - \omega_{\mathbf{q}s}) d\mathbf{q}, \tag{13}$$

which can be summed up to the total DOS. The total phonon spectrum with contributions from each vibrational mode (i.e., different colored lines under the total DOS curve) can be observed in Fig. 5(a).

The comparison between the current ENDF/B-VIII.0 library for YH_2, (Zerkle and Holmes, 2017) and the s-TDEP calculated phonon spectrum can be observed in Fig. 5(b). The ENDF/B-VIII.0 phonon spectrum was notably calculated by using VASP and PHONON codes with a lattice constant of 5.2032 Å. The ENDF/B-VIII.0 library uses the same phonon spectrum to generate the thermal scattering law at different temperatures from 293.6 to 1,600 K. The goal of this work is to use TDEP to calculate the temperature dependence of the phonon spectrum and compare it with the experiments. s-TDEP-calculated phonon spectra at different temperatures can be observed in Fig. 5(c).

Section 4.1.2 details the discussion regarding the differences between s-TDEP phonon spectra at different temperatures and the comparison with ENDF/B-VIII.0 phonon spectrum, aided by comparison with the measurements.

4. Results

4.1. SEQUOIA and ARCS

4.1.1. Experimental data

A plot that shows the effect of temperature on the inelastic spectra of $YH_{1.86}$ is shown in Fig. 6. To better compare multiple experiments in one plot, the dynamic structure factor is integrated over *Q*-space and normalized to unity. The large peak at energy

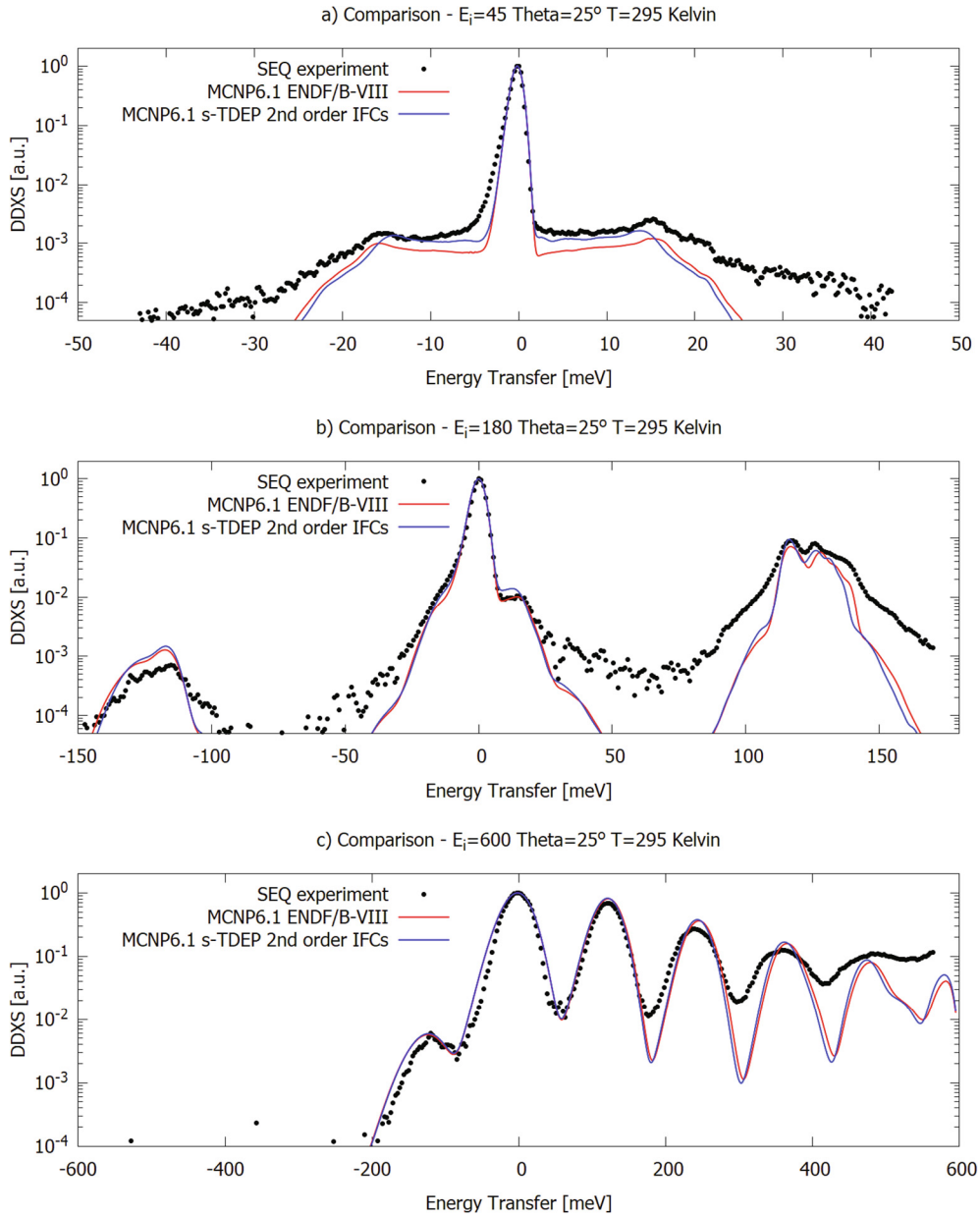

Fig. 13. DDXS comparison between ENDF/B-VIII.0 and s-TDEP against SEQUOIA measured data at 295 K, 25° scattering angle, and 45, 180, and 600 meV incident energies.

transfer = 0 represents the elastic peak and is an expected feature. For all of these plots, the experimental uncertainties are too small to be displayed on the plots unless stated otherwise and thus are not shown. Additionally, plots of the 2D dynamic structure factor at each incident energy at 5 K are shown in Fig. 7.

This work shows the expected features of the dynamic structure factor as temperature is increased, primarily that the higher temperature modes broaden out at positive energy transfer and a more pronounced mode at negative energy transfer. This is due to the difference in one-phonon scattering as a function of positive or negative energy transfer, described by:

$$S(Q,E>0) \sim e^{-u_H^2(T)Q^2}[n(E,T)+1],$$
$$S(Q,E<0) \sim e^{-u_H^2(T)Q^2}[n(E,T)], \quad (14)$$

where $u_H^2(T)$ is the mean squared displacement of hydrogen atoms, $e^{-u_H^2(T)Q^2}$ is the Debye Waller factor, and $n(E,T)$ is the Bose population factor defined by:

$$n(E,T) = \left[e^{E/k_BT} - 1\right]^{-1}. \quad (15)$$

The Bose population factor increases with temperature, but $n(E,T)$ will increase relatively more for neutron energy gain sites (E<0) than $[n(E,T)+1]$ for neutron energy lost sites (E > 0) because $n(E,T)$ is almost zero at low temperature (T = 5 K).

Figs. 6(a) and 6(b) also show how the peak between 10 to 20 meV (i.e., the yttrium contribution to the spectra) increases as temperature increases, whereas the peaks between 100 to 150 meV (i.e., hydrogen contributions) decrease. Since the bound scattering cross section of hydrogen is much larger than for yttrium (82.02 b vs. 7.7 b) and the dynamic structure factor is inversly proportional to atomic mass, the spectra is mainly due to the scattering off of hydrogen. The 10–20 meV peak corresponds to yttrium vibrations, which cause hydrogen atoms to vibrate, whereas the 100–150 meV range corresponds solely to hydrogen vibrations. Since the Debye Waller factor for hydrogen is almost the same for all energies, this also due to the Bose population factor

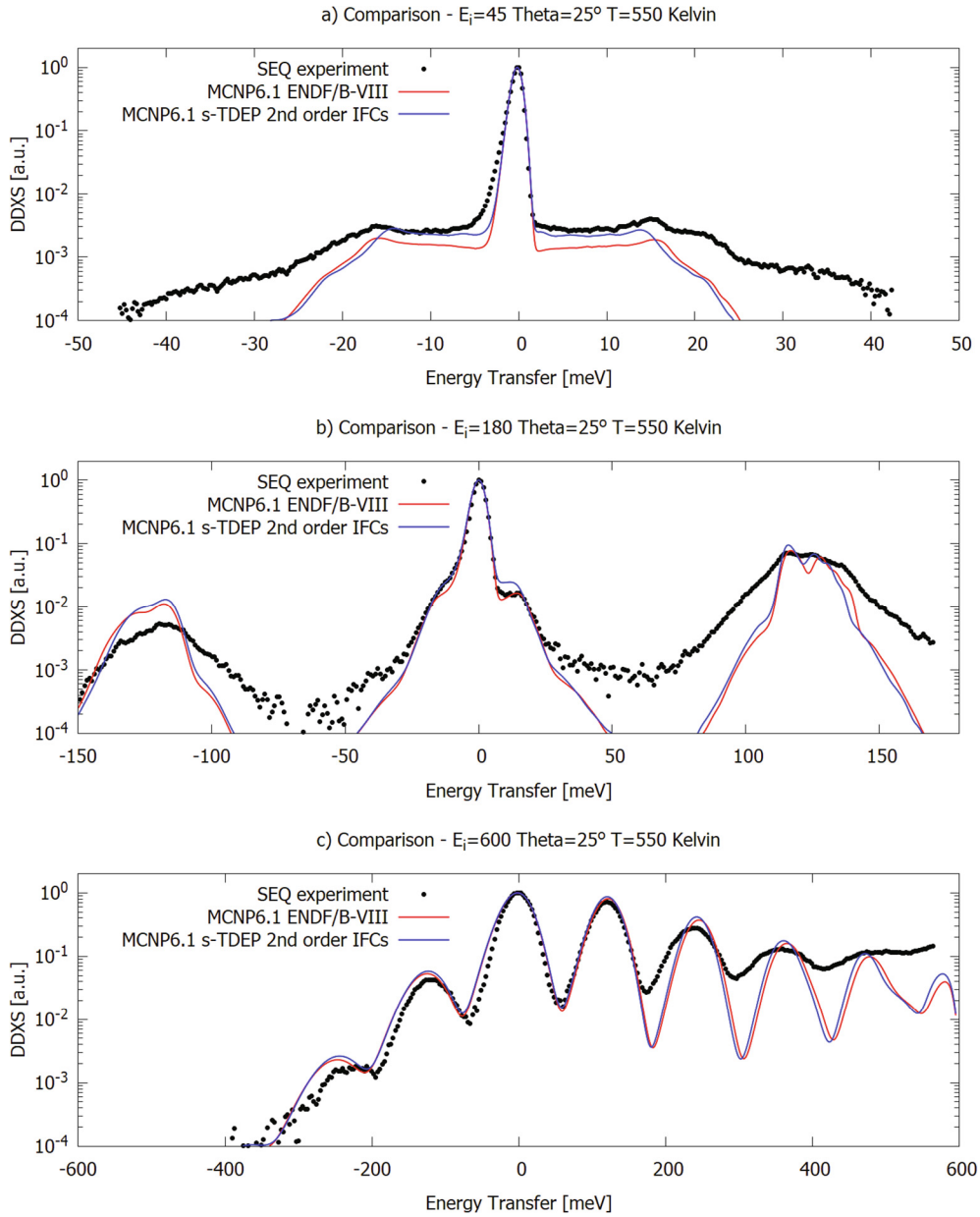

Fig. 14. DDXS comparison between ENDF/B-VIII.0 and s-TDEP against SEQUOIA measured data at 550 K, 25° scattering angle, and 45, 180, and 600 meV incident energies.

contributions since the Bose population factor has a larger impact on the 10–20 meV range than on the 100–150 meV range. All three plots also show that increasing temperature changes the location of some of the peaks. This is most noticeable in the 600 meV plot between 100 to 150 meV. This is due to changes in the lattice constants as a function of temperature, as discussed in Section 3.3.

A plot showing the Q-integrated spectra as a function of hydrogen concentration at 180 meV and 5 K is shown in Fig. 8. From this plot, there appears to be only a small difference between the two different hydrogen concentrations. There could be a difference between the two in that the $YH_{1.62}$ has a larger peak around the 10–15 meV range and smaller peaks in the 100–150 meV range compared with $YH_{1.86}$. Since the spectra are both normalized to unity, this indicates that the alpha yttrium contribution is more prominent in samples with smaller hydrogen concentration. Also, since hydrogen is mostly contained in the delta phase, the real formula for the hydride phase should be delta-$YH_{1.81}$ for $YH_{1.62}$ and delta-$YH_{1.93}$ for $YH_{1.86}$. Therefore, the difference in hydrogen concentrations in the delta phases is 6.6%.

The INS spectra from the ARCS beamline as a function of temperature are shown in Fig. 9. Again, the shifting of the peak locations noticed from the SEQUOIA measurements is shown, albeit more prominently since the maximum temperature of the ARCS experiments was 1,200 K. A comparison of the ARCS and SEQUOIA data for the same temperature and incident energy is shown in Fig. 10 in which the range of Q-values available from ARCS are shown to be different compared with the range from SEQUOIA due to the wider angular array of detectors at ARCS. Another plot comparing the spectra measured at the two spectrometers is shown in Fig. 11 in which the Q-integrated spectra between the two are shown to be comparable with a few exceptions. The elastic peak is wider in the ARCS data because ARCS generally has a broader energy resolution. This can also be seen in the E_i = 180 meV plot at around 20 meV in which the acoustic peak is more

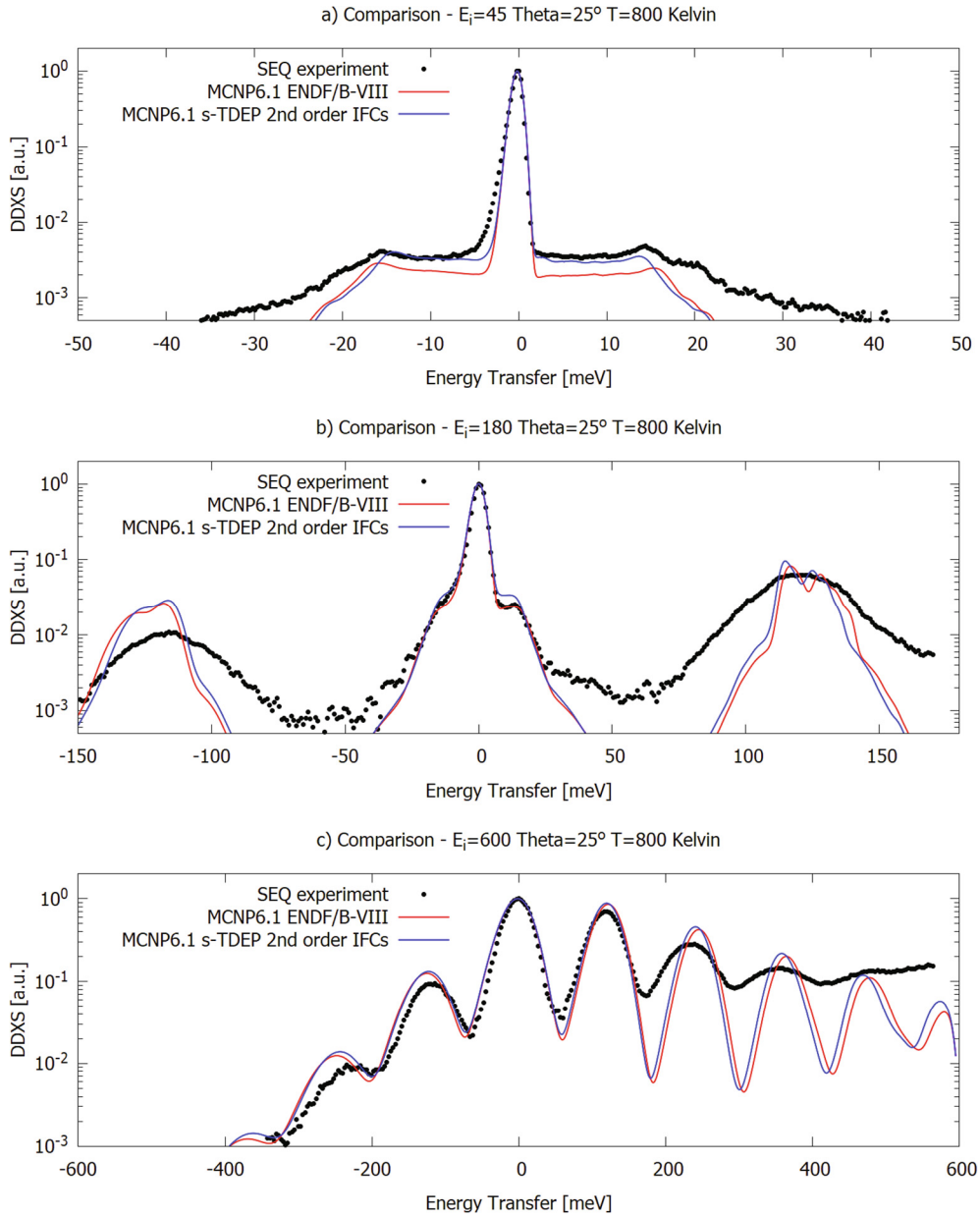

Fig. 15. DDXS comparison between ENDF/B-VIII.0 and s-TDEP against SEQUOIA measured data at 800 K, 25° scattering angle, and 45, 180, and 600 meV incident energies.

noticeable in the SEQUOIA data than the ARCS data. Because of these reasons, simulation of the 5, 295, 550, and 800 K data will be compared against SEQUOIA measurements. A comparison against the ARCS measurements at all measured temperatures will be presented in a follow-up paper.

4.1.2. Simulation of measured data

To compare the experimental data, ENDF/B-VIII.0 library, and s-TDEP calculated library, the SEQUOIA experimental setup was simulated in MCNP6.1 (Goorley and James, 2013), as was done in Chapman et al. (2021) and Ramic et al. (2018) and Ramic et al. (2019). An improved resolution function was implemented in comparison with the previous model that used a Gaussian resolution function. A neutron beam profile at each incident energy was calculated by using MCViNE (Lin et al., 2016), which was used as an input to the MCNP6.1 calculation, and the respective resolution parameters for the SEQUOIA instrument were applied to the DDXS obtained from MCNP6.1. Thermal scattering libraries at different temperatures in ACE format for MCNP6.1 were calculated from respective phonon spectra with NJOY2016.

Figs. 12–15 show the comparison between the experiments and MCNP-calculated DDXS from ENDF/B-VIII.0 and s-TDEP phonon spectra at 5, 295, 550, and 800 K. In these plots, the experimental uncertainties are not shown due to the logarithmic scaling of the DDXS. Figs. 12(a), 13(a), 14(a), and 15(a) show that the acoustic peak locations are slightly under-calculated. This can also be observed in the comparison between ENDF/B-VIII.0 and the s-TDEP phonon spectra in Fig. 5(b). From Figs. 12(a), 13(a), 14(a), and 15(a), it can also be inferred that the locations of the acoustic peaks are shifted to lower energies with the rising temperature and thus are over-calculated by the ENDF/B-VIII.0 library at higher temperatures. The shifts in the acoustic phonon peak locations as a function temperature with E_i = 45 meV can be also observed in Figs. 6(a) and 9(a). At 180 meV incident energy, Figs. 6(b), and 9 (b) also show shifts in the optical peaks to lower energy (i.e., "softening") as the temperature increases from 295 to 1200 K.

Each data trend, from 5 to 800 K, can be observed in s-TDEP-calculated phonon spectra in Fig. 5(c)—although 5 and 295 K phonon spectra slightly under-calculate the location of the first peak in the optical region in comparison with the experimental data—and in the DDXS calculated data in FIgs. 12(b), 13(b), 14(b), and 15(b). At 600 meV incident energy, the multiple phonon scattering contributions to DDXS spectra are observed. From Figs. 12(c), 13(c), 14(c), and 15(c), the fundamental mode with a peak around 130 meV is observed to be calculated correctly, whereas the overtones are slightly shifted to higher energies. This is mostly due to the anharmonicity of YH_x, which is not replicated by the LEAPR module of NJOY2016. When calculating multiple phonon contributions, LEAPR convolutes the fundamental mode phonon spectrum with itself. In Figs. 12(b), 13(b), 14(b), and 15(b), the authors noted that they should be able to observe the shifts of optical peaks to lower energies as temperature increases, but that is even more pronounced in Figs. 12(c), 13(c), 14(c), and 15(c). The trend can be observed in the first fundamental peak around 130 meV but is even more clear in the overtones in which the shift to lower energies is more pronounced.

4.2. VISION

4.2.1. Experimental data

Results from the VISION experiment at 5 K as a function of the hydrogen concentration are shown in Fig. 16. A plot that shows the change in spectra as a function of temperature is shown in Fig. 17. In these plots, each dataset is normalized to a proton charge, which correlates to the number of neutrons impinging on the sample.

From these plots, there is no noticeable difference between the samples as a function of hydrogen concentration in the magnitude of the peaks or their location. There is evidence to suggest that the potential well for hydrogen in YH_x is anharmonic at energy transfers greater than 300 meV. To further show this, the high-Q data at 5 K are plotted against multiphonon spectra calculated in the harmonic approximation (Li and Kolesnikov, 2002) and the Sjölander approximation (Sjölander, 1958) by using the spectra in the range of the fundamental modes (i.e., the spectra between E = 0 to

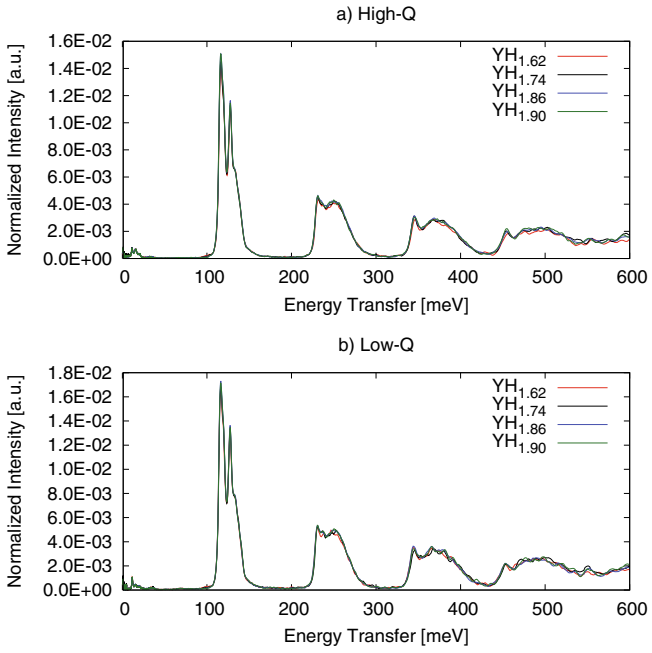

Fig. 16. Hydrogen concentration comparison of VISION data of YH_x for x = 1.62, 1.74, 1.86, and 1.90 at 5 K.

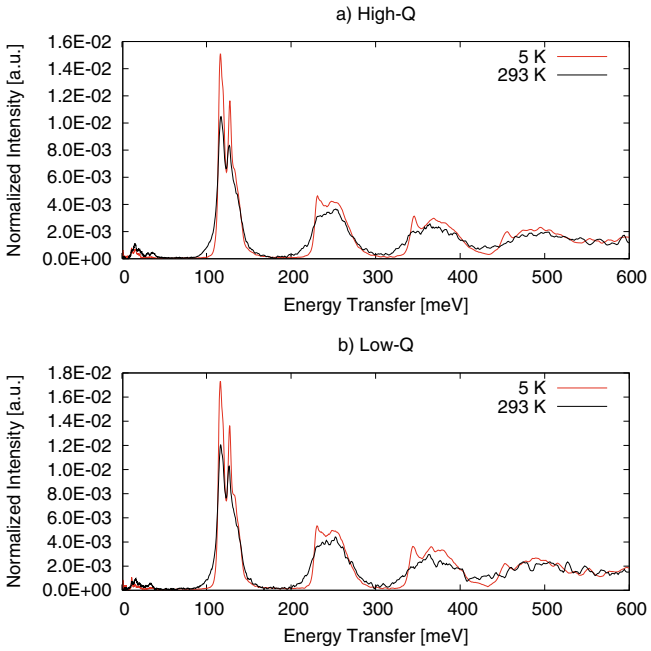

Fig. 17. Temperature comparison of VISION data of $YH_{1.86}$ at 5 and 293 K.

150 meV) in Fig. 18. There is a significant red shift of the lower peaks, as indicated by the arrows, compared with the harmonic approximation calculations.

4.2.2. Simulation data

Unlike the ARCS and SEQUOIA simulations, the VISION simulation data can be extracted directly from the dynamic structure factor calculated for analysis in Section 4.1.2. This is due to the fact that, unlike ARCS and SEQUOIA, there are only two spectra to simulate corresponding to the two scattering angles (forward and backward) as opposed to ARCS and SEQUOIA, which have a range of scattering angles to simulate. After applying the VISION detector resolution function, the resulting spectrum can be directly compared with the experimental data. These results are shown in Fig. 19. The magnitudes of the simulated peaks agree favorably with the VISION data with two notable exceptions: (1) the second peak of the fundamental mode near E = 130 meV and (2) the magnitude of the anharmonic peaks denoted by the arrows in Fig. 18. Overall, there is a slight shift of the s-TDEP results toward the correct location of the peaks; however, much like the ARCS and SEQUOIA comparison, the differences between the ENDF/B-VIII.0 and s-TDEP results are small. This could indicate that more advanced methods are needed to calculate the multiphonon scattering contributions to the overall spectra.

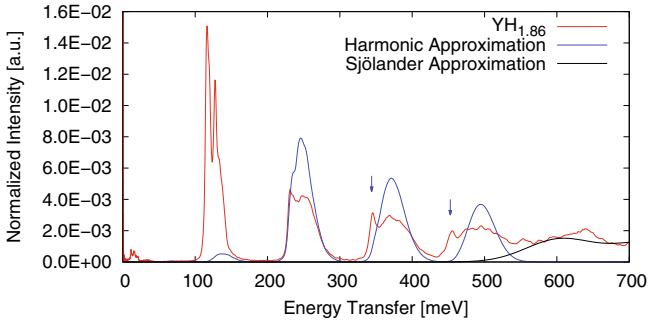

Fig. 18. Comparison of VISION high-Q 5 K experimental data with multiphonon harmonic and Sjölander approximations.

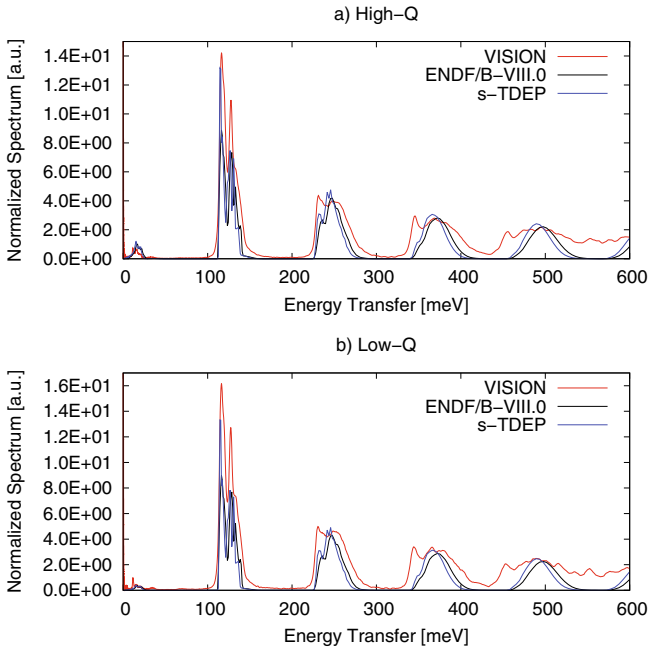

Fig. 19. Comparison of VISION data against ENDF/B-VIII.0 and s-TDEP for $YH_{1.86}$ at 5 K.

5. Conclusions and future work

The dynamic structure factors of yttrium hydride with H/Y atomic ratios from 1.62 to 1.90 were measured with the SEQUOIA, ARCS, and VISION instruments at SNS in the temperature range of 5 to 1,200 K to capture the temperature and hydrogen concentration dependence. The VISION measurement of the selected YH_x samples indicated anharmonic effects. These experiments provide a platform to validate the currently available ENDF/B-VIII.0 thermal scattering files and demonstrate the need for more accurate thermal scattering files to capture the temperature broadening and anharmonic effects. This work showed that the s-TDEP method can be used to calculate the temperature dependence of the phonon spectrum for $YH_{\sim 2}$ samples. The method correctly predicts the softening of optical peaks from 295 to 800 K.

The acoustic peaks are slightly under-calculated, and denser $7 \times 7 \times 7$ k-points force calculations will be performed for the follow-up paper via VASP to check whether it will lead to improvement. The phonon spectra used in this work were calculated from only second-order IFCs. The follow-up work will present the results from phonon spectra obtained by using third- and fourth-order IFCs, which can be calculated via the TDEP method. A study on including nuclear quantum effects will also be performed with contributions from second-, third-, and fourth-order IFCs. Additionally, s-TDEP calculations will be performed for temperatures up to 1,200 K that are complementary to the ones done in this work up to 800 K. Modeling and comparison with ARCS experimental data will be also performed with an improved input file that will better replicate the full ARCS detector setup. Thermodynamic quantities will also be calculated at all temperatures, such as specific heat capacity, mode Gruneisen parameters, and lattice thermal conductivity.

One phenomena that was briefly mentioned involves the location of the hydrogen atom in the YH_x lattice. At room temperature, the location is known to favor the tetrahedral sites in the delta-YH_2 lattice, but it is unclear how this changes as a function of temperature. It is also possible that some of the higher temperature spectra might be described by new vibrational states in the phonon DOS. This will be investigated with the higher order, high-temperature s-TDEP calculations.

CRediT authorship contribution statement

Chris W. Chapman: Methodology, Software, Investigation, Writing - original draft, Writing - review & editing, Visualization. **Kemal Ramić:** Methodology, Software, Writing - original draft, Writing - review & editing, Visualization. **Xunxiang Hu:** Conceptualization, Methodology, Resources, Writing - original draft, Writing - review & editing, Funding acquisition, Project administration. **Jesse M. Brown:** Investigation, Writing - review & editing. **Goran Arbanas:** Investigation, Writing - original draft, Writing - review & editing, Supervision. **Alexander I. Kolesnikov:** Investigation, Writing - review & editing. **Douglas L. Abernathy:** Investigation, Writing - review & editing. **Luke Daemen:** Investigation, Writing - review & editing. **Anibal (Timmy) J. Ramirez-Cuesta:** Software, Investigation, Writing - review & editing, Resources. **Yongqiang Cheng:** Software, Investigation, Writing - review & editing. **Matthew B. Stone:** Investigation, Writing - review & editing. **Li (Emily) Liu:** Resources, Writing - review & editing. **Yaron Danon:** Resources, Writing - review & editing.

Declaration of Competing Interest

The authors declare that they have no known competing financial interests or personal relationships that could have appeared to influence the work reported in this paper.

Acknowledgments

The authors would like to thank Dr. Olle Hellman for the help with s-TDEP method, as well as Victor Fanelli, Bekki Mills, and Andrew Payzant for their help in planning and coordinating the SNS experiments.

This research was sponsored by the Transformational Challenge Reactor Program of the US Department of Energy Office of Nuclear Energy.

This research used resources of the Compute and Data Environment for Science at ORNL, which is supported by DOE SC under Contract No. DE-AC05-00OR22725.

This research used resources at the Spallation Neutron Source, a DOE Office of Science User Facility operated by the Oak Ridge National Laboratory.

This research used resources of the National Energy Research Scientific Computing Center, a DOE SC user facility operated under Contract No. DE-AC02-05CH11231.

Computational resources were also provided by the Rensselaer Polytechnic Institute Center for Computational Innovations, more specifically the Artificial Intelligence Multiprocessing Optimized System supercomputer.

References

Advanced Small Modular Reactors, 2017. Department of Energy. https://www.energy.gov/ne/nuclear-reactor-technologies/small-modular-nuclear-reactors

Begun, G.M., Land, J.F., Bell, J.T., 1980. High temperature equilibrium measurements of the yttrium-hydrogen isotope (H2, D2, T2) systems. J. Chem. Phys. 72 (5), 2959–2966. https://doi.org/10.1063/1.439496.

Betzler, B., Ade, B., Wysocki, A., Jain, P., Chesser, P., Greenwood, M., Terrani, K., 2020. Transformational challenge reactor preconceptual core design studies. Nucl. Eng. Des. 367,. https://doi.org/10.1016/j.nucengdes.2020.110781. http://www.sciencedirect.com/science/article/pii/S0029549320302752 110781.

Abernathy, D.L., 2008. ARCS: a wide Angular-Range Chopper Spectrometer at the SNS, Notiziario Neutroni E Luce di Sincrotrone 13 (1). URL: https://www.osti.gov/biblio/963378.

D. Brown, M. Chadwick, R. Capote, A. Kahler, A. Trkov, M. Herman, A. Sonzogni, Y. Danon, A. Carlson, M. Dunn, D. Smith, G. Hale, G. Arbanas, R. Arcilla, C. Bates, B. Beck, B. Becker, F. Brown, R. Casperson, J. Conlin, D. Cullen, M.-A. Descalle, R.

Firestone, T. Gaines, K. Guber, A. Hawari, J. Holmes, T. Johnson, T. Kawano, B. Kiedrowski, A. Koning, S. Kopecky, L. Leal, J. Lestone, C. Lubitz, J. Márquez Damián, C. Mattoon, E. McCutchan, S. Mughabghab, P. Navratil, D. Neudecker, G. Nobre, G. Noguere, M. Paris, M. Pigni, A. Plompen, B. Pritychenko, V. Pronyaev, D. Roubtsov, D. Rochman, P. Romano, P. Schillebeeckx, S. Simakov, M. Sin, I. Sirakov, B. Sleaford, V. Sobes, E. Soukhovitskii, I. Stetcu, P. Talou, I. Thompson, S. van der Marck, L. Welser-Sherrill, D. Wiarda, M. White, J. Wormald, R. Wright, M. Zerkle, G. Žerovnik, Y. Zhu, ENDF/B-VIII.0: The 8th Major Release of the Nuclear Reaction Data Library with CIELO-project Cross Sections, New Standards and Thermal Scattering Data, Nuclear Data Sheets 148 (2018) 1 – 142, special Issue on Nuclear Reaction Data. doi:https://doi.org/10.1016/j.nds.2018.02.001. URL: http://www.sciencedirect.com/science/article/pii/S0090375218300206.

Chapman, C.W., Arbanas, G., Kolesnikov, A.I., Leal, L., Danon, Y., WendorffRamic, C.K., Liu, L., Rahnema, F., 2021. Methodology for generating covariance data of thermal neutron scattering cross sections. Nuclear Science and Engineering.

Daou, J.N., Vajda, P., 1992. Hydrogen ordering and metal-semiconductor transitions in the system YH_{2+x}. Phys. Rev. B 45, 10907–10913. https://doi.org/10.1103/PhysRevB.45.10907.

Elsässer, C., Schweizer, S., Fähnle, M., 1996. Hydrogen Vibration in Cubic Dihydrides MH2 (M=Ti, Zr), and Localization in Cubic Laves Phases ZrM2H1/2 (M=V, Cr, Fe, Co). MRS Proceedings 453, 221. https://doi.org/10.1557/PROC-453-221.

Fu, K., Jiang, X., Guo, Y., Li, S., Zheng, J., Tian, W., Li, X., 2018. Experimental investigation and thermodynamic assessment of the yttrium-hydrogen binary system. Progress Natural Sci.: Mater. Int. 28 (3), 332–336. https://doi.org/10.1016/j.pnsc.2018.04.001. URL: http://www.sciencedirect.com/science/article/pii/S1002007117309747.

Goorley, J., James, M. et al., 2013. Initial MCNP6 Release Overview, Tech. Rep. LA-UR-13-22934, Los Alamos National Laboratory..

Goret, G., Aoun, B., Pellegrini, E., 2017. MDANSE: An Interactive Analysis Environment for Molecular Dynamics Simulations, Journal of Chemical Information and Modeling 57 (1) (2017) 1–5, pMID: 28026944. arXiv: https://doi.org/10.1021/acs.jcim.6b00571, doi:10.1021/acs.jcim.6b00571. URL: doi: 10.1021/acs.jcim.6b00571..

Granroth, G.E., Kolesnikov, A.I., Sherline, T.E., Clancy, J.P., Ross, K.A., Ruff, J.P.C., Gaulin, B.D., Nagler, S.E., 2010. J. Phys: Conf. Ser. 251,. https://doi.org/10.1088/1742-6596/251/1/012058 012058.

Hacene, M., Anciaux-Sedrakian, A., Rozanska, X., Klahr, D., Guignon, T., Fleurat-Lessard, P., 2012. Accelerating VASP electronic structure calculations using graphic processing units, J. Comput. Chem. 33 (32) (2012) 2581–2589. arXiv: https://onlinelibrary.wiley.com/doi/pdf/10.1002/jcc.23096, doi:10.1002/jcc.23096. URL: https://onlinelibrary.wiley.com/doi/abs/10.1002/jcc.23096..

Hellman, O., Abrikosov, I.A., 2013. Temperature-dependent effective third-order interatomic force constants from first principles. Phys. Rev. B 88,. https://doi.org/10.1103/PhysRevB.88.144301 144301.

Hellman, O., Abrikosov, I.A., Simak, S.I., 2011. Lattice dynamics of anharmonic solids from first principles. Phys. Rev. B 84,. https://doi.org/10.1103/PhysRevB.84.180301 180301.

Hellman, O., Steneteg, P., Abrikosov, I.A., Simak, S.I., 2013. Temperature dependent effective potential method for accurate free energy calculations of solids. Phys. Rev. B 87,. https://doi.org/10.1103/PhysRevB.87.104111 104111.

Hu, X., Schappel, D., Silva, C.M., Terrani, K.A., 2020. Fabrication of yttrium hydride for high-temperature moderator application. J. Nucl. Mater. 539,. https://doi.org/10.1016/j.jnucmat.2020.152335. URL: http://www.sciencedirect.com/science/article/pii/S0022311520305456 152335.

Hutchinson, M., Widom, M., 2012. VASP on a GPU: Application to exact-exchange calculations of the stability of elemental boron. Comput. Phys. Commun. 183 (7), 1422–1426. https://doi.org/10.1016/j.cpc.2012.02.017. URL: http://www.sciencedirect.com/science/article/pii/S0010465512000707.

Khatamian, D., Kamitakahara, W.A., Barnes, R.G., Peterson, D.T., 1980. Crystal structure of $YD_{1.96}$ and $YH_{1.98}$ by neutron diffraction. Phys. Rev. B 21, 2622–2624. https://doi.org/10.1103/PhysRevB.21.2622. URL: https://link.aps.org/doi/10.1103/PhysRevB.21.2622.

Khatamian, D., Manchester, F., 1988. The H - Y (hydrogen-yttrium) system. Bulletin of Alloy Phase Diagrams 9 (3), 252–260. https://doi.org/10.1007/BF02881276.

Kim, D.S., Hellman, O., Herriman, J., Smith, H.L., Lin, J.Y.Y., Shulumba, N., Niedziela, J. L., Li, C.W., Abernathy, D.L., Fultz, B., 2018. Nuclear quantum effect with pure anharmonicity and the anomalous thermal expansion of silicon. Proc. Nat. Acad. Sci. 115 (9), 1992–1997. https://doi.org/10.1073/pnas.1707745115. URL: https://www.pnas.org/content/115/9/1992.

Kresse, G., Furthmüller, J., 1996. Efficiency of ab-initio total energy calculations for metals and semiconductors using a plane-wave basis set. Comput. Mater. Sci. 6 (1), 15–50. https://doi.org/10.1016/0927-0256(96)00008-0. URL: http://www.sciencedirect.com/science/article/pii/0927025696000080.

Kresse, G., Furthmüller, J., 1996. Efficient iterative schemes for ab initio total-energy calculations using a plane-wave basis set. Phys. Rev. B 54, 11169–11186. https://doi.org/10.1103/PhysRevB.54.11169. URL: https://link.aps.org/doi/10.1103/PhysRevB.54.11169.

Kresse, G., Hafner, J., 1993. Ab initio molecular dynamics for liquid metals. Phys. Rev. B 47, 558–561. https://doi.org/10.1103/PhysRevB.47.558. URL: https://link.aps.org/doi/10.1103/PhysRevB.47.558.

Li, J., Kolesnikov, A.I., 2002. Neutron spectroscopic investigation of dynamics of water ice. J. Mol. Liq. 100 (1), 1–39.

Lin, J.Y., Smith, H.L., Granroth, G.E., Abernathy, D.L., Lumsden, M.D., Winn, B., Aczel, A.A., Aivazis, M., Fultz, B., 2016. MCViNE - An object oriented Monte Carlo neutron ray tracing simulation package. Nucl. Instrum. Methods Phys. Res., Sect. A 810, 86–99. https://doi.org/10.1016/j.nima.2015.11.118. URL: http://www.sciencedirect.com/science/article/pii/S0168900215015053.

MacFarlane, R., Kahler, A., 2010. Methods for Processing ENDF/B-VII with NJOY, Nuclear Data Sheets 111 (12) (2010) 2739–2890, Nuclear Reaction Data. doi:10.1016/j.nds.2010.11.001. URL: http://www.sciencedirect.com/science/article/pii/S0090375210001006..

Niedziela, J.L., Mills, R., Loguillo, M.J., Skorpenske, H.D., Armitage, D., Smith, H.L., Lin, J.Y.Y., Lucas, M.S., Stone, M.B., Abernathy, D.L., 2017. Design and operating characteristic of a vacuum furnace for time-of-flight inelastic neutron scattering measurements. Rev. Sci. Instrum. 88, (10). https://doi.org/10.1063/1.5007089 105116.

Parlinski, K., 2007. J. Phys: Conf. Ser. 92,. https://doi.org/10.1088/1742-6596/92/1/012009 012009.

Parlinski, K., 2018. Ab initio determination of anharmonic phonon peaks. Phys. Rev. B 98,. https://doi.org/10.1103/PhysRevB.98.054305 054305.

Ramic, K., Wendorff, C., Cheng, Y., Kolesnikov, A.I., Abernathy, D.L., Daemen, L., Arbanas, G., Leal, L., Danon, Y., Liu, L.E., 2018. Thermal scattering law of C2H4n: Integrating experimental data with DFT calculations. Ann. Nucl. Energy 120, 778–787. https://doi.org/10.1016/j.anucene.2018.06.029. URL: http://www.sciencedirect.com/science/article/pii/S030645491830330X.

Ramic, K., Wendorff, C., Cheng, Y., Kolesnikov, A.I., Abernathy, D.L., Daemen, L., Arbanas, G., Leal, L., Danon, Y., Liu, L.E., 2019. Toward a better thermal scattering law of (C5O2H8)n: Inelastic neutron scattering and oClimax + NJOY2016. Ann. Nucl. Energy 133, 425–430. https://doi.org/10.1016/j.anucene.2019.05.042. URL: http://www.sciencedirect.com/science/article/pii/S0306454919302956.

Seeger, P.A., Daemen, L.L., Larese, J.Z., 2009. Resolution of VISION, a Crystal-Analyzer Spectrometer. Nucl. Instrum. Methods Phys. Res., Sect. A 604 (3), 719–728. https://doi.org/10.1016/j.nima.2009.03.204. URL: http://www.sciencedirect.com/science/article/pii/S0168900209006871.

Shulumba, N., Hellman, O., Minnich, A.J., 2017. Intrinsic localized mode and low thermal conductivity of PbSe. Phys. Rev. B 95,. https://doi.org/10.1103/PhysRevB.95.014302 014302.

Sjölander, A., 1958. Multi-phonon Processes in Slow Neutron Scattering by Crystals. Arkiv för Fysik 14 (4), 315–371.

Tadano, T., Gohda, Y., Tsuneyuki, S., 2014. J. Phys.: Condens. Matter 26, (22). https://doi.org/10.1088/0953-8984/26/22/225402 225402.

Togo, A., Tanaka, I., 2015. First principles phonon calculations in materials science. Scr. Mater. 108, 1–5.

Udovic, T.J., Rush, J.J., Anderson, I.S., 1994. Local-mode dynamics in YH_2 and YD_2 by isotope-dilution neutron spectroscopy. Phys. Rev. B 50, 15739–15743. https://doi.org/10.1103/PhysRevB.50.15739. URL: https://link.aps.org/doi/10.1103/PhysRevB.50.15739.

Wang, W.-E., Olander, D.R., 1995. Thermodynamics of the Zr-H System. J. Am. Ceram. Soc. 78 (12), 3323–3328.

Villars, Pierre (Chief Editor): YH2 Crystal Structure: Datasheet from "PAULING FILE Multinaries Edition – 2012" in SpringerMaterials (https://materials.springer.com/isp/crystallographic/docs/sd_0559145), copyright Springer-Verlag, Berlin Heidelberg & Material Phases Data System (MPDS), Switzerland & National Institute for Materials Science (NIMS), Japan, 2016.

Zerkle, Michael, Holmes, Jesse, 2017. A thermal neutron scattering law for yttrium hydride, EPJ Web Conf. 146 (2017) 13005. doi:10.1051/epjconf/201714613005. URL: https://doi.org/10.1051/epjconf/201714613005.